

Article

Irradiance Impact on Pollution by Integrating Nephelometer Measurements

Maria Rita Perrone *, Pasquale Burlizzi and Salvatore Romano

Received: 30 October 2015; Accepted: 2 December 2015; Published: 8 December 2015

Academic Editor: Daniele Contini

Dipartimento di Matematica e Fisica, Università del Salento, Via per Arnesano, 73100 Lecce, Italy; pasquale.burlizzi@le.infn.it (P.B.); salvatore.romano@unisalento.it (S.R.)

* Correspondence: perrone@le.infn.it; Tel.: +39-0832-297-498; Fax: +39-0832-297-592

Abstract: Three-wavelength integrating nephelometer measurements combined with short- (SW) and long-wave (LW) irradiance measurements were used to investigate the irradiance effects on the daily evolution of the particulate matter (PM) at the ground level, and contribute to the characterization of the land–atmosphere interaction in pollution dispersal. The integrating nephelometer measurements have allowed characterizing the daily changes of the PM optical and microphysical properties by the aerosol scattering coefficient (σ_p) and the scattering Ångström coefficient (\AA). We found that on a daily basis σ_p reached the minimum values when the irradiance reached the maximum values, since the convective motions, which favor the particle dispersion at the surface, increase with the irradiance. The \AA value, which is commonly used as qualitative indicator of the dominant particle size, has allowed evaluating the irradiance effects on the mean particle size distribution at the surface and revealed that the irradiance increase favors mainly the dispersion of the ground-level fine particles. Particle size-distribution measurements supported the last comment. Measurements were performed from 4 to 10 May 2015 when the study site was affected by a Saharan dust outbreak, to also evaluate the impact of long-range transported particles on the daily evolution of the ground-level particle’s properties and the SW and LW irradiance.

Keywords: air pollution; integrating nephelometer measurements; short-wave irradiance; long-wave irradiance; desert dust

1. Introduction

Ground-level aerosol properties depend on the local sources of particles, the impact of the long-range transboundary air pollution, and the local meteorology [1]. A good knowledge of the aerosol optical properties is required to characterize their interaction with the radiation and evaluate their impact on climate. Multi-wavelength integrating nephelometers are currently used to characterize the particle scattering properties [2]. In particular, the nephelometers allow measuring particle scattering (σ_p) and hemispheric backscattering (β_p) coefficients at different wavelengths and calculating the scattering Ångström coefficients (\AA), which are commonly used as a qualitative indicator of the dominant particle size [3]. Lyamani *et al.* [4] found in Granada, an urban site in southeastern Spain, that the aerosol scattering coefficient was characterized by a marked seasonal dependence with maxima in winter, and a clear diurnal pattern in all seasons, which was attributed to the diurnal evolution of the planetary boundary layer (PBL) and to local anthropogenic activities. Pereira *et al.* [5] reported aerosol scattering measurements performed at Évora, Portugal, over seven years (2002–2008). They found that both seasonal and daily cycles of the scattering and backscattering coefficients were related to the local production and transport of particles from elsewhere. Multi-wavelength nephelometer measurements performed at a coastal site of southeastern

Italy, from December 2011 to November 2012, were reported by Perrone *et al.* [6]. They also found that the σ_p and β_p values and their respective dependence on wavelength were strongly dependent on airflows. In particular, they showed that the *in situ* particle properties and the local meteorological parameters varied with the advection routes. Given the dependence of \hat{a} and β_p/σ_p on the particle size and shape, it was found that \hat{a} and β_p/σ_p values allowed a satisfactory differentiation of the particle optical properties associated with different advection routes. Columnar and ground-level aerosol optical properties from sun/sky photometer and nephelometer measurements, respectively, collocated in space and time were analyzed in [1]. It was found that the large impact of the local meteorology on the daily evolution of the ground-level aerosol properties was mainly responsible for the weak correlation of the ground-level parameters with the corresponding columnar parameters.

Multi-wavelength integrating nephelometer measurements combined with short- and long-wave irradiance measurements have been analyzed in this study to investigate the effects of the short- and long-wave radiation on the daily evolution of the aerosol scattering properties at the surface and obtain a better understanding of the factors affecting the σ_p daily cycle. It is also a main goal of the study to contribute to the characterization of the land–atmosphere interaction in pollution dispersal. In particular, the relationships between radiative fluxes and aerosol optical and microphysical properties have been investigated in this study, unlike previous works. The surface radiation budget, which is affected by the clouds and the aerosol load, drives the strong diurnal surface cycle over land, as it is well known [7]. The scattering Ångström coefficient, calculated from the scattering coefficient measurements, and particle size measurements have been used to trace the daily changes of the mean particle size distribution and evaluate the irradiance effects on the particle dispersal. This work focused on measurements taken from 4 to 10 May 2015, since the study site was strongly affected by a Saharan dust outbreak on some of the selected measurement days. Therefore, the selected period has also allowed investigating the impact of transboundary particles on the daily cycle of the short- and long-wave radiative fluxes and the aerosol optical and microphysical properties. Measurements from the AERONET (AErosol RObotic NETwork) sun/sky photometer [8] operating at the study site were used to characterize the columnar aerosol properties and obtain a better understanding of the daily cycle of the irradiance and the particle properties at the surface. Model results from the Barcelona Supercomputing Center Dust REgional Atmospheric Model (BSC-DREAM8b v2.0 model) were used to trace the dust particle vertical profiles [9].

2. Sampling Site and Instruments

2.1. Site Description

The nephelometer measurements were performed on the roof of the Mathematics and Physics Department of the University of Salento, at about 10 m above ground level (AGL). The Mathematics and Physics Department is located in a flat suburban area (40.33°N; 18.11°E) of the Salento peninsula of Italy, at 30 m above sea level. It is about 6 km away from the town of Lecce (96,000 inhabitants) and about 20 km from both the Ionic and Adriatic Seas (Figure 1). The monitoring site of this study may be considered as representative of coastal sites of the Central Mediterranean away from large sources of local pollution [10].

2.2. Instrumentation Description

Particle scattering and hemispheric backscattering coefficients at 450, 525, and 635 nm were measured by a LED-based integrating nephelometer (model Aurora 3000, ECOTECH, Knoxfield, Australia) at a temporal resolution of five minutes. Air sampling was obtained from the top of a stainless steel tube, 15 mm internal diameter and about 1.5 m length. The inlet was fitted with a funnel covered by a screen to prevent rain drops and insect from getting into the sample line. The automatic processor-controlled heater inside the nephelometer has allowed setting the internal relative humidity threshold at 40% to prevent hygroscopic effects enhancing the particle scattering

properties. The full calibration of the device was carried out every two months using CO₂ as high span gas and internally filtered free air (particle with a diameter < 0.1 μm) as low span gas. Calibration checks were regularly performed on a weekly basis in order to detect any drift in the nephelometer’s calibration. The nephelometer includes backscatter measurements that allow both standard integrating and hemispheric measurements from 9° to 170°. Müller *et al.* [11] have provided a detailed description of the instrument and the factors to correct systematic uncertainties due to angular truncation and non-Lambertian illumination. More specifically, correction factors for total scatter as function of the Ångström coefficients, calculated from uncorrected scattering coefficients, were used [11].

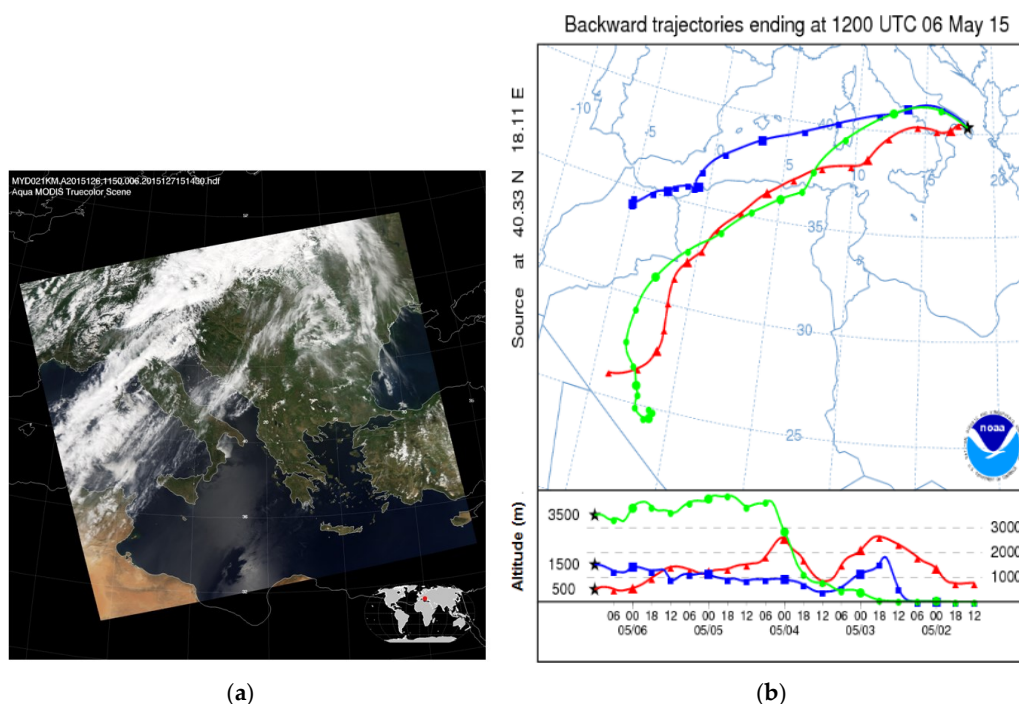


Figure 1. (a) True color image from MODIS (Moderate Resolution Image Spectroradiometer) on board the Aqua satellite at 11:50 a.m. UTC on 6 May 2015; (b) Five-day HYSPLIT (HYbrid Single Particle Lagrangian Integrated Trajectory) back trajectories that reached the monitoring site at 12:00 p.m. UTC on 6 May 2015, at 0.5 (red), 1.5 (blue), and 3.5 km (green) AGL.

Two Kipp & Zonen pyranometers (CMP 21 model) and two pyrgeometers (CGR 3 model) were used to retrieve upward and downward radiative flux at the surface in the short-wave (SW, 0.31–2.8 μm) and in the long-wave (LW, 4.5–42 μm) spectral range, respectively. The CMP 21 pyranometer presents a non-linearity <0.2% in the range 100–1000 Wm⁻², a directional response <10 Wm⁻² (up to 80° with 1000 Wm⁻² beam) and a temperature response <1% (from -20 to +50 °C). The CGR 3 pyrgeometer has a non-linearity <1% and a temperature response <5% (from -40 to +40 °C). Collected data were averaged over two minutes and stored for subsequent analysis. The total uncertainty associated with the CMP 21 pyranometer and the CGR 3 pyrgeometer measurements is 2% and 3%, respectively, taking into account temperature, calibration and cosine error of the devices. Both devices are located at about 10 m from the ground.

For continuous aerosol size distribution measurements, an Aerodynamic Particle Sizer (APS) model 3321 from TSI was deployed at about 10 m from the ground. It is an optical particle counter that measures the particle diameter in 51 channels of equal logarithmic width within the 0.52–20.0 μm range by determining the time-of-flight of individual particles in an accelerating flow field. APS operated at flow rate of 5 l min⁻¹ and with data averaging time of 30 min.

Measurements from the AERONET sun/sky photometer operating since 2003 at the monitoring site and denoted as “Lecce University” were used to characterize the columnar aerosol properties. The CIMEL sun/sky photometer measures by two automatic detectors the direct solar flux in eight channels between 340 and 1020 nm and the diffuse-sky flux in four channels between 440 and 1020 nm. The instantaneous values of the aerosol optical depth and the columnar Ångström coefficient used in this study were derived from direct solar flux measurements [8]. Only sun/sky photometer measurements performed under clear-sky conditions (cloud-screened) and quality-assured data (level 2.0) were used.

3. Results and Discussion

The nephelometer and radiometer measurements analyzed in this Section were performed from 4 to 10 May 2015 since southeastern Italy was strongly affected by a Saharan dust outbreak on some days of the monitoring period. The selected days have hence allowed investigating the transboundary pollution impact on the daily cycle of the analyzed parameters, as previously mentioned. An overview of the dust outbreak evolution is first presented in the Section. To this end, AERONET direct sun photometer measurements, MODIS (MODerate resolution Image Spectroradiometer; satellite images [12], analytical back-trajectories from the HYSPLIT (HYbrid Single Particle Lagrangian Integrated Trajectory) model [13], and dust concentration profiles from the BSC-DREAM8b model [9] have been used. The daily evolution of the particle scattering coefficient, the scattering Ångström coefficient, and the SW- and LW-irradiance from 4 to 10 May 2015 are then presented to provide an overview of the daily variability of the investigated parameters. Finally, the measurements performed on 6 and 8 May are analyzed in more detail, since 6 and 8 May were strongly and weakly affected, respectively, by the desert dust advection.

3.1. Characterization of the Dust Outbreak Evolution at the Study Site

Figure 1a shows, as an example, the true color image from MODIS on board the Aqua satellite at 11:50 a.m. UTC on 6 May revealing a huge amount of dust particles over the Central Mediterranean basin. The red dot on Figure 1a represents the study site. The five-day HYSPLIT back trajectories that reached the monitoring site at 12:00 p.m. UTC on 6 May and at 0.5, 1.5, and 3.5 km AGL are plotted on Figure 1b. One observes that the advected air masses were originated over northwestern Africa. The instantaneous values of the aerosol optical depth (AOD) at 440 nm, retrieved from the AERONET direct sun photometer measurements performed from 4 to 10 May, have been used to trace the evolution of the columnar aerosol load (Figure 2, open black dots). The columnar Ångström coefficient (Å) was used as a qualitative indicator of the dominant particle size [3]. In fact, coarse mode particles as desert dust and sea-salt lead to Å values close to zero, while fine mode particles as the ones due to the anthropogenic pollution lead to Å values larger than one. The open grey triangles on Figure 2 show the instantaneous values of Å calculated at the 440–870 nm wavelength pair by the following relationship [1]:

$$\text{Å}(440, 870 \text{ nm}) = -\ln((\text{AOD}(440 \text{ nm})/(\text{AOD}(870 \text{ nm}))/(\ln(440/870))) \quad (1)$$

A discussion on the uncertainties of the AERONET aerosol products is provided in [14]. Figure 2 reveals that the AOD and Å values were characterized by a rather high day-to-day variability. The AOD values varied within the 0.09–0.15 and the 0.38–0.48 range on 4 and 6 May, respectively. Note that 6 May was the day most affected by Saharan dust during the analyzed period. On the contrary, the Å values that were larger than 1.2 on 4 May (dust-free day) decreased up to about 0.2 on 6 May because of the Saharan dust advection. The dust concentration vertical profiles from the BSC-DREAM8b model for the monitoring site of this study were used to have some information on the daily changes of the dust load distribution up to the ground level. Figure 3 shows the dust concentration as a function of the height above sea level at 12:00 a.m. (black solid line), 6:00 a.m.

(black dotted line), 12:00 p.m. (grey solid line), and 6:00 p.m. UTC (grey dotted line) of (a) 4, (b) 5, (c) 6, (d) 7, (e) 8, (f) 9, and (g) 10 May, respectively. One observes that 4 May was very weakly affected by dust particles, while 6 May was the day most affected by dust particles throughout the day, in good accordance with the AERONET retrievals (Figure 2). Dust particles that were located at altitudes smaller than 1 km at 12:00 p.m. UTC of 4 May (Figure 3a, grey solid line) extended up to about 6 km on 5 (Figure 3b), 6 (Figure 3c), and 7 May (Figure 3d). One also observes from Figure 3b–d that the dust load and the corresponding vertical profile varied significantly with the day hours, in good accordance with the AOD time evolution (Figure 2, open black dots). The high daily and day-to-day variability of the dust particle AOD and of the particle vertical distribution resulting from Figures 2 and 3 respectively, is typical of dust outbreaks, in accordance with lidar measurements performed at the study site [15]. Note that both AERONET (Figure 2) and model results (Figure 3) indicate that the dust advection was nearly over on 10 May.

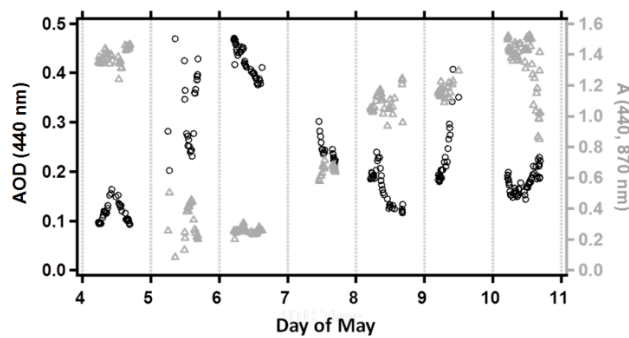


Figure 2. Temporal evolution of the instantaneous values of the AOD (Aerosol Optical Depth) at 440 nm (open black dots) and of the columnar Ångström coefficient calculated at the 440–870 nm wavelength pair (open grey triangles) from AERONET (Aerosol Robotic Network) direct sun measurements, from 4 to 10 May 2015.

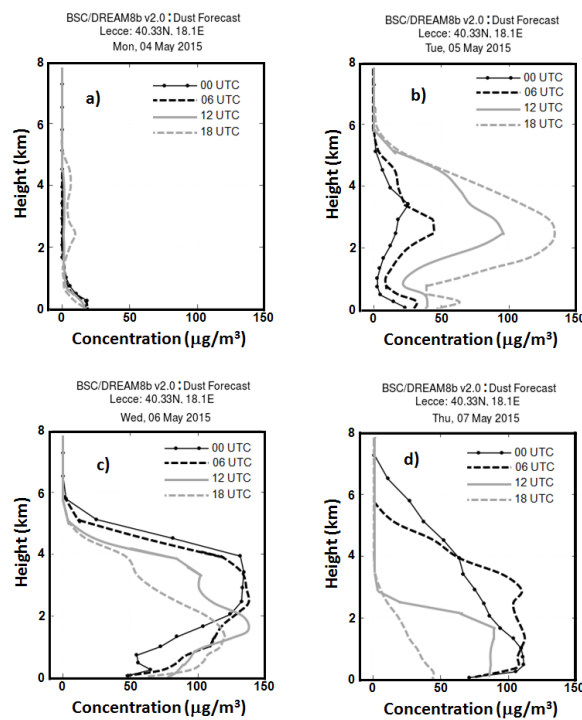


Figure 3. Cont.

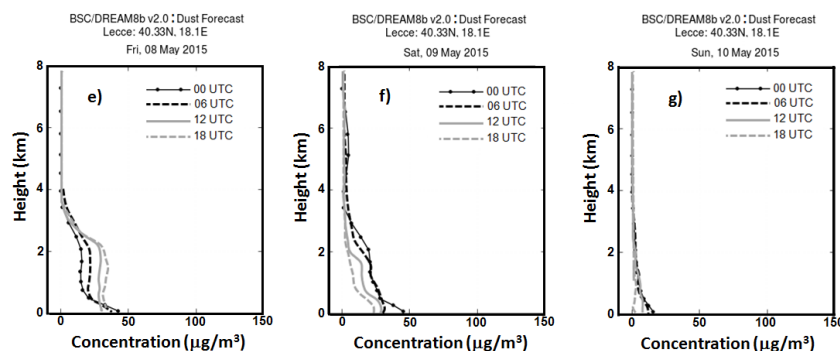


Figure 3. Dust concentration *versus* the height above sea level at 12:00 a.m. (black solid line), 6:00 a.m. (black dotted line), 12:00 p.m. (grey solid line), and 6:00 p.m. UTC (grey dotted line) of (a) 4, (b) 5, (c) 6, (d) 7, (e) 8, (f) 9, and (g) 10 May 2015, respectively, from the BSC-DREAM8b model.

3.2. Radiative Fluxes and Particle Scattering Coefficients from 4 to 10 May 2015

Radiometer and nephelometer measurements referring to the studied period are presented in this sub-section to provide an overview of their spanning range and day-to-day variability, and to highlight main effects of the daily variability of the SW and LW irradiance on the particle scattering properties at the surface. Figure 4 (grey lines) shows the time evolution of the two hour-averaged (a) SW downward flux ($SW-F_{DW}$), (b) LW downward flux ($LW-F_{DW}$), and (c) LW upward flux ($LW-F_{UP}$) with the corresponding Standard Errors of the Mean (SEM). The time evolution of the SW upward flux has not been shown since it was quite similar to the $SW-F_{DW}$ to less than the surface albedo multiplicative factor. The solar zenith angle, the surface albedo, the aerosol optical and microphysical properties (mainly AOD, particle size distribution, asymmetry parameter, and SSA), which in turn depend on the particle composition and mixing state [16], and the cloud properties represent some of the most important parameters affecting the irradiance and its daily cycle. Note that the AERONET AODs (Figure 2) were retrieved under clear sky conditions from 4:45 a.m. to 4:40 p.m. UTC of each day. Therefore, any lack of AERONET AOD values was due to the presence of clouds. Consequently, the AOD values allow identifying the clear sky daytime hours. Open dots on Figure 4 show the instantaneous AODs (440 nm) to highlight the aerosol load impact on the irradiance measurements at the surface. In particular, Figure 4a reveals that smaller $SW-F_{DW}$ peak values were reached on the days characterized by greater AODs. The $SW-F_{DW}$ peak value, which was equal to 941 Wm^{-2} around 12:00 p.m. UTC of 4 May, decreased down to 930 Wm^{-2} (about 1% decrease) around 12:00 p.m. UTC of 6 May because of the desert dust advection and, consequently, the AOD (440 nm) increase from 0.15 up to 0.40, which corresponds to the AOD increase by a factor 2.7. Note that Romano *et al.* [17] found that an AOD (675 nm) increase of about a factor of five determined a $SW-F_{DW}$ decrease of 9% at the same site of this study, by analyzing the 9–13 July 2012 dust outbreak. Figure 4c also reveal that greater $LW-F_{DW}$ and $-F_{UP}$ peak values, respectively, were reached on the days characterized by greater AOD values. In particular, the $LW-F_{UP}$ and $-F_{DW}$ peak values that were equal to 540 and 384 Wm^{-2} , respectively, around 12:00 p.m. UTC of 4 May increased up to 567 and 395 Wm^{-2} around 12:00 p.m. UTC of 6 May, respectively, because of the AOD increase by a factor 2.7. The absorption [18] and the scattering effects [19] of desert dust particles in the LW domain enhance the greenhouse effect by trapping the outgoing terrestrial radiation and, consequently, may lead to greater $LW-F_{DW}$ (Figure 4b) and $LW-F_{UP}$ (Figure 4c) values. However, one must be aware that the LW irradiance is also dependent on the effective radiating temperatures and emissivity of both the atmosphere and the surface, while it is less affected by surface albedo and solar zenith angle (SZA) changes with respect to the SW irradiance [20]. Consequently, we found that the daily evolution of the $LW-F_{DW}$ was characterized by a less regular daily cycle than the $SW-F_{DW}$.

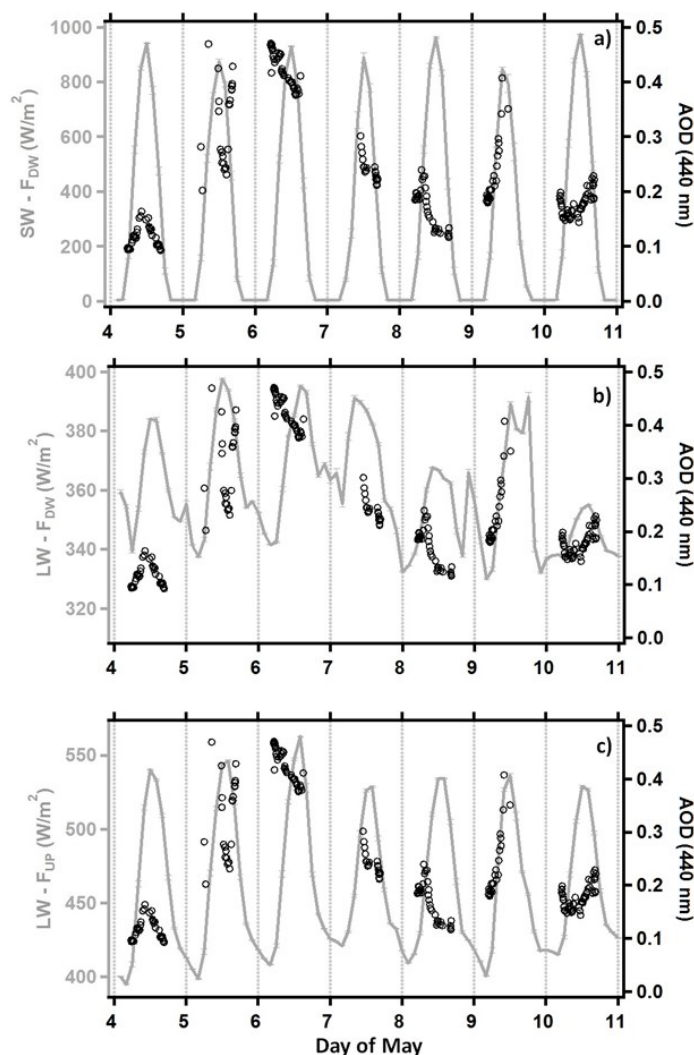


Figure 4. The grey lines show the time evolution of the two hour-averaged (a) short-wave downward flux (SW-F_{DW}), (b) long-wave downward flux (LW-F_{DW}), and (c) long-wave upward flux (LW-F_{UP}) from 4 to 10 May 2015. Error bars represent the SEMs (standard errors of the mean). Open dots represent the instantaneous AOD (440 nm) values from AERONET direct sun measurements.

Figure 5a (black line) shows the time evolution of the particle scattering coefficient at 450 nm averaged over 2 hours with corresponding SEM from 4 to 10 May 2015. σ_p values that spanned the 37–245 Mm⁻¹ range were characterized by a rather high daily and day-to-day variability, because of the high variability of the optical and microphysical properties of the atmospheric particles due to both the local production and the long-range transport. Scattering coefficients depend on the number concentration, the size, the shape, and the absorption of the sampled particles. The changes of the synoptic and local meteorological conditions, which affect the optical and microphysical properties of particles, also have a large impact on the σ_p daily cycle and variability [1,6], in addition to the particle’s source changes. The grey line on Figure 5a shows the time evolution of the two hour-averaged scattering Ångström coefficient values with corresponding SEMs. The scattering Ångström coefficient at the 450–635 nm wavelength pair was calculated from the following relation [1]:

$$\hat{a}(450, 635 \text{ nm}) = -\ln ((\sigma_p(450 \text{ nm})/(\sigma_p(635 \text{ nm}))/(\ln (450/635))) \tag{2}$$

and describes the σ_p spectral dependence. \hat{a} , a qualitative indicator of the dominant particle size, spanned the 0.1–1.6 range, indicating that also the contribution of fine and coarse mode particles at the

ground level significantly varied during the studied period. The rather low \hat{a} values around midday of 6 May and around 10:00 p.m. UTC on 7 May were likely due to the large dust concentration near the ground level, in accordance with the modeled dust vertical profiles of Figure 3c,d, respectively. Figure 5a shows also that small \hat{a} values were on average associated with small σ_p values. The σ_p decrease with the particle size increase and, hence, with the \hat{a} decrease has likely contributed to this last result. Note that the σ_p decrease may also be associated with the decrease of the fine-mode particle contribution, as it will be shown in the following. Figure 5b shows the σ_p (450 nm) versus \hat{a} (450, 635 nm) plot. The data points have been fitted with a linear regression. The linear correlation coefficient R that is equal to 0.49 and the corresponding significance level that is larger than 99% indicate that the two parameters were satisfactorily correlated. The data spread revealed by Figure 5b mainly at $\hat{a} > 1$ was due to the variability of the particle concentration, being σ_p and \hat{a} an extensive and an intensive particle parameter, respectively.

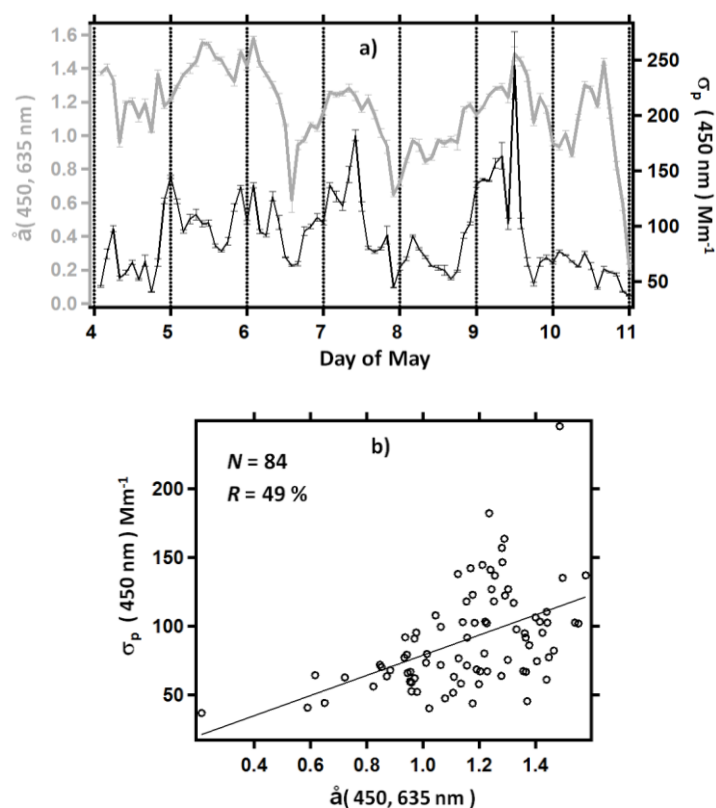


Figure 5. (a) The black and grey lines show the 2-hour averaged values of σ_p (450 nm) and \hat{a} (450, 635 nm), respectively, retrieved from nephelometer measurements, from 4 to 10 May 2015. Error bars represent the SEMs; (b) σ_p (450 nm) versus \hat{a} (450, 635 nm) plot. The solid line represents the best fitting regression line, N is the total number of data, and R represents the linear correlation coefficient.

The σ_p time evolution has been compared with the one of the SW- F_{DW} , LW- F_{DW} , and LW- F_{UP} on Figure 6a–c, respectively, to highlight the irradiance effects on the σ_p daily changes and, hence, on the ground level particle properties. One observes from Figure 6 that on each day σ_p reached on average the smallest values around noon, when the SW and LW fluxes reached the highest values. The high irradiance values around noon, which favor the air convective motions and hence the dispersion of the atmospheric particles at the surface, were responsible for these results. The high σ_p values monitored around midday of 7 and 9 May were likely due to the advection of a large amount of fine mode particles, being the σ_p values associated with \hat{a} values larger than 1.2 (Figure 5a). Figure 6 also reveals that σ_p on average increased at night-time when the SW and LW irradiance reached minimum

values and the air convective motions decreased, favoring the particle accumulation at the ground level. Surface wind speed and direction measurements from a local meteorological station have also been used to obtain a better understanding of the σ_p daily evolution from 4 to 10 May. Figure 7 (grey lines) shows the time evolution of the two hour-averaged (a) wind speed and (b) direction from 4 to 10 May 2015. The σ_p daily evolution is also shown on each plot of Figure 7 for comparison (black lines). One observes at first from Figure 7a that the wind speed on average reached largest values around midday when the SW and LW irradiances also reached peak values. Consequently, Figure 7a reveals that σ_p decreased (increased) with the increase (decrease) of the wind speed, since the wind speed affected the vertical dispersion of the ground-level aerosols [1].

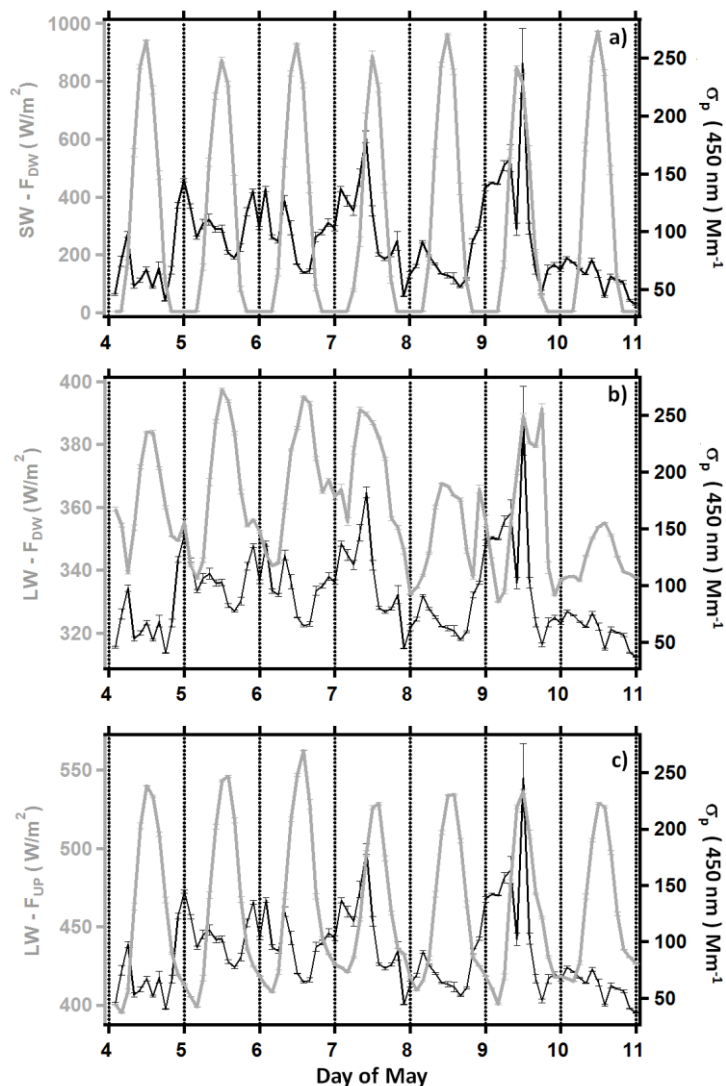


Figure 6. Comparison of the time evolution of the two hour-averaged σ_p (black line) with one of (a) SW-F_{DW} (grey line), (b) LW-F_{DW} (grey line), and (c) LW-F_{UP} (grey line), from 4 to 10 May 2015. The error bars represent the corresponding SEMs.

Figure 7b allows inferring that the σ_p daily evolution might also be affected by the surface wind direction. In fact, Figure 7b (grey line) shows that the wind direction daily cycle that was rather similar on 4, 5, and 6 May, changed day-to-day since midday of 7 May. Then, Figure 7b (black line) reveals that the σ_p daily cycle was characterized by a greater day-to-day variability on 8, 9, and 10 May than on 4, 5, and 6 May.

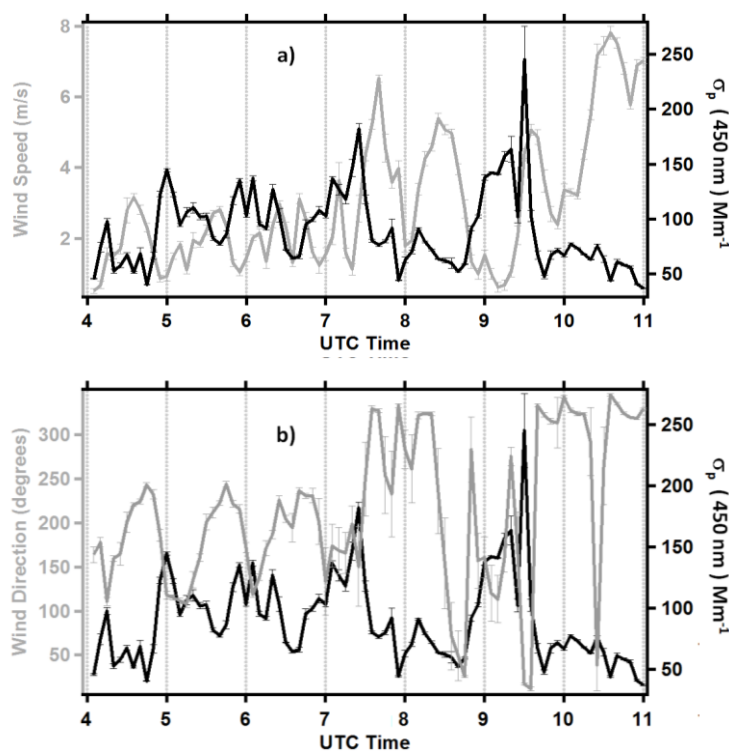


Figure 7. Time evolution of the two-hour averaged values of (a) wind speed (grey line) and σ_p (black line), and (b) wind direction (grey line) and σ_p (black line). The error bars represent the corresponding SEMs.

3.3. Scattering and Irradiance Measurements on 6 and 8 May 2015: Case Studies

The daily evolution of the SW and LW irradiance and of the aerosol scattering coefficient monitored on 6 and 8 May are analyzed in more detail in this subsection to present and discuss the irradiance impact on the dispersion and the size distribution of the surface particles, by two case studies. The Saharan dust advection was largest on 6 May and weak on 8 May, as the columnar Ångström coefficient values of Figure 2 (triangles) indicate. Figure 8a shows the time evolution of the two hour-averaged σ_p (black solid line), SW- F_{DW} (black dotted line), and LW- F_{DW} (grey solid line) on 6 May 2015. The time evolution of the two hour-averaged scattering Ångström coefficient is plotted on Figure 8b (black line). The grey line on Figure 8b shows the time evolution of the two hour-averaged LW- F_{UP} . The σ_p peak value around 2:00 a.m. UTC, revealed by Figure 8a (black solid line), was likely due to the advection of a “cloud” of fine mode particles of anthropogenic origin. To support the last comment, note that Å (450, 635 nm) reached the peak value of 1.6 around 2:00 a.m. UTC (Figure 8b, black solid line) and then decreased. In fact, Å values larger than one are observed when fine mode particles are dominant, as mentioned. Figure 8a also shows that σ_p reached a peak value around 8:00 a.m. UTC and, then, rapidly decreased with the time up to about 2:00 p.m. UTC. The σ_p decrease was associated with the fast increase of the SW and LW irradiance, which favored the planetary boundary layer increase and, hence, the particle dispersion. Figure 8b (black line) reveals that Å also decreased with the time reaching the minimum value of 0.6 at around 2:00 p.m. UTC, when the LW- F_{DW} and - F_{UP} reached the maximum value. The combined decrease of both the σ_p and the Å values could be due to several processes. It would be possible that the increased irradiance resulted in a more vigorous and turbulent convection, which favored the mixing of the upper air enriched with long range transported African dust particles, with the air below containing mostly fine particles. This would result in an overall reduction of the scattering coefficient through dilution, and an increase of the fraction of larger particles with respect to the smaller ones. Note that 6 May

was a clear sky day characterized by a large amount of coarse mode particles due to African dust up to the ground level (Figure 3c). The irradiance increase could also have favored more the dispersion of the fine mode particles than that of the coarse mode particles, being the latter on average “heavier” than fine mode particles. Vehicles, which enhance the re-suspension of road dust (large particles) into the air on the diurnal traffic rush hours, could also have contributed to the decrease around midday as mentioned in some studies [4]. Size distribution measurements at the surface support the decrease of the fine-mode particle contribution with the increase of the SW and LW irradiance, as is shown in the following.

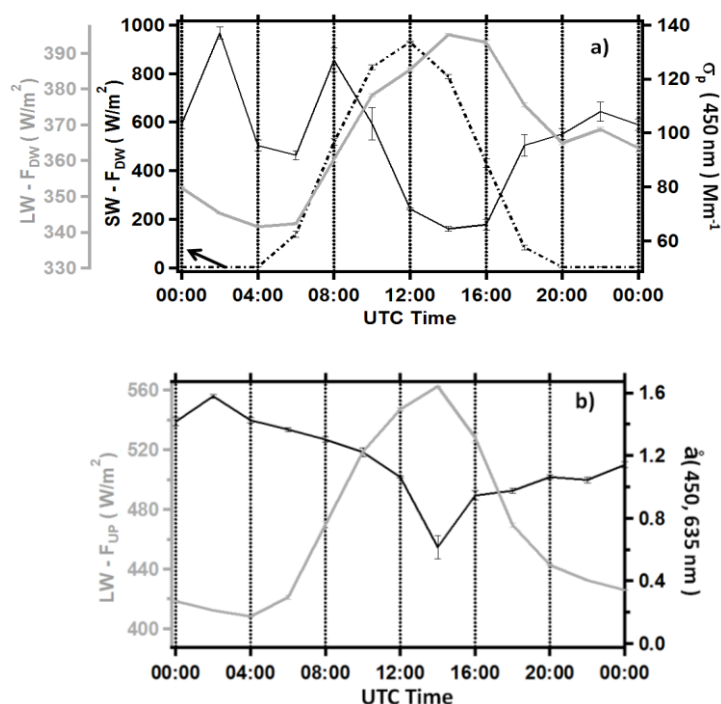


Figure 8. (a) Daily evolution of the two hour-averaged values of σ_p (black solid line), SW-F_{DW} (black dotted line), and LW-F_{DW} (grey solid line) on 6 May 2015; (b) Two hour-averaged λ (450, 635 nm) (black line) and LW-F_{UP} (grey line) daily evolution on 6 May 2015. The error bars represent the corresponding SEMs.

Figure 9 shows the aerosol size distributions within the 0.52–20 μm range obtained at different day hours on 6 May from the APS 3321 measurements averaged over 30 min. More specifically, Figure 9a,b show the number (N) and the volume (V) particle concentrations, respectively, as a function of the particle diameter (D_p) on a logarithmic scale. Note that the volume particle concentrations are commonly used to highlight the contribution of coarse mode particles, which have a number concentration significantly smaller than the one of fine mode particles, as Figure 9a reveals. One observes from Figure 9a that the number concentration of the fine mode particles rapidly decreased reaching a rather small value around 1:30 p.m. UTC. On the contrary, it increased reaching a large value around 8:30 p.m. UTC, when the SW and LW irradiance reached minimum values and favored the particle accumulation at the surface because of the decrease of the planetary boundary layer height. In addition, Figure 9b shows that the volume concentration of the coarse mode particles at the surface increased with the fine mode particle decrease and *vice versa*. Note that the time evolution of the size distribution revealed by Figure 9a,b is in good accordance with the λ temporal trend of Figure 8b (black line).

Figure 10 shows the time evolution of the two hour-averaged σ_p (black solid line), SW-F_{DW} (black dotted line), and LW-F_{DW} (grey solid line) on 8 May 2015. Observe that σ_p reached a peak value

around 4:00 a.m. UTC, decreased with the increase of the SW and LW irradiance reaching a minimum value around 4:00 p.m. UTC, and increased fast with the time after sunset. Therefore, one can note from Figure 10 (black solid line) that the σ_p daily evolution on 8 May (day weakly affected by dust) was similar to the one on 6 May (dusty day) from sunrise to sunset, as revealed by the comparison with Figure 8a (black solid line). This last outcome indicates that the desert dust advection on 6 May has not determined a significant variation of the σ_p daily cycle, since the latter was mostly dependent on the diurnal evolution of the irradiance and, hence, of the planetary boundary layer height. The number (N) and volume (V) particle concentrations *versus* the particle diameter (D_p) at different day hours are shown in Figure 11a,b, respectively. In particular, Figure 11a reveals that the number concentration of the fine particles decreased/increased with the σ_p decrease/increase. Conversely, Figure 11b reveals that the volume concentration of the coarse particles increased with the σ_p decrease. As mentioned, several factors have likely contributed to the increase (decrease) of the coarse (fine) particle contribution. We believe that the presented results highlight the large effects of the local SW and LW irradiance on the land–atmosphere interaction and particle dispersion even when the local pollution at the surface was largely affected by the contribution of transboundary particles.

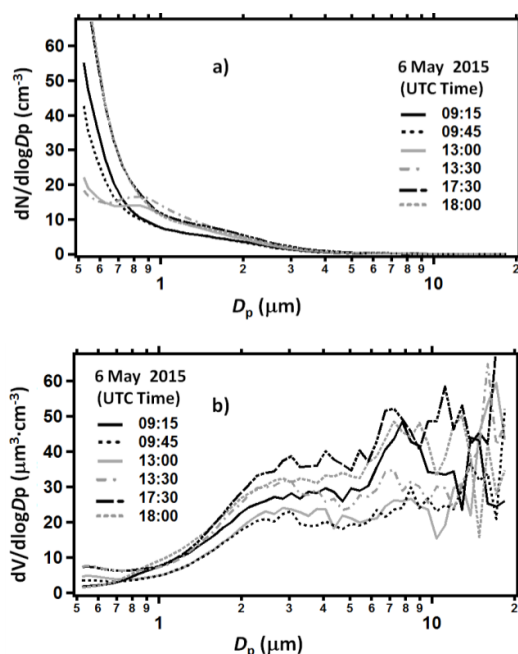


Figure 9. (a) Number (N) and (b) volume (V) particle concentrations *versus* the particle diameter (D_p) on a logarithmic scale within the 0.52–20 μm range at different day hours on 6 May 2015.

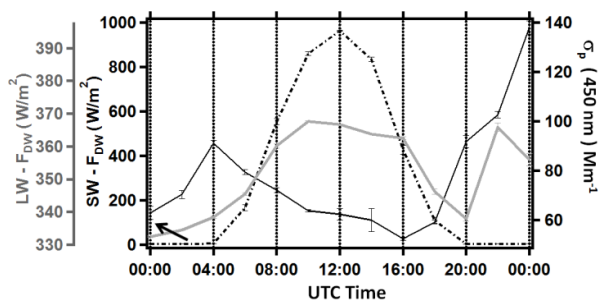


Figure 10. Daily evolution of the two hour-averaged values of σ_p (black solid line), SW-F_{DW} (black dotted line), and LW-F_{DW} (grey solid line) on 8 May 2015. The error bars represent the corresponding SEMs.

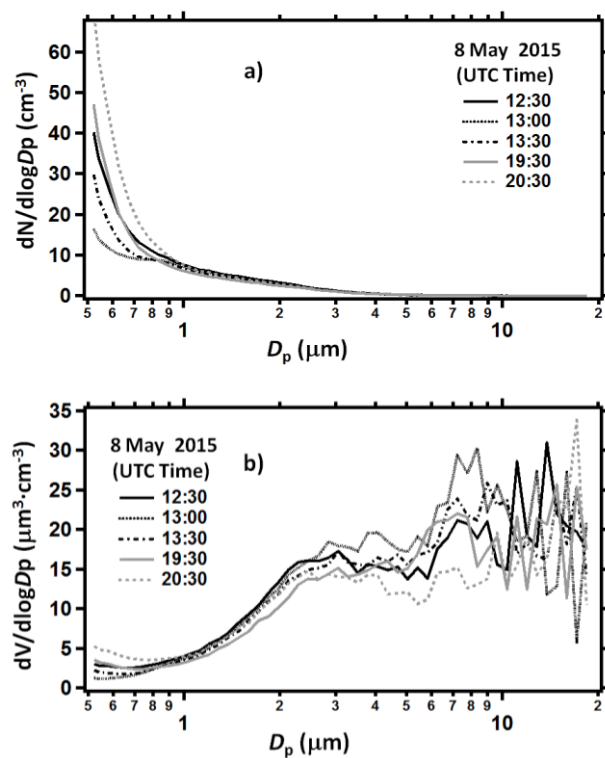


Figure 11. (a) Number (N) and (b) volume (V) particle concentrations *versus* the particle diameter (D_p) on a logarithmic scale within the 0.52–20 μm range at different day hours on 8 May 2015.

4. Summary and Conclusion

The irradiance effects on the optical and microphysical properties of the ground level particles and, hence, on the particle dispersion at the surface have been analyzed. More specifically, integrating nephelometer measurements combined with short- and long-wave irradiance measurements were used to investigate the relationships between radiative fluxes and aerosol optical and microphysical properties at the surface and contribute to the characterization of the land–atmosphere interaction in pollution dispersal. The study focused on the measurements performed from 4 to 10 May 2015, since southeastern Italy was strongly affected by a Saharan dust outbreak on some days of the monitoring period. Therefore, the selected days have also allowed investigating the SW and LW irradiance effects on the land-atmosphere interaction during some days largely affected by the contribution of transboundary particles. Aerosol scattering coefficients at 450 nm and scattering Ångström coefficients from nephelometer measurements were used to trace the hourly and daily changes of the aerosol optical properties at the surface, in addition to size distribution measurements. It has been shown that the surface particle concentration was strongly affected by both the SW and LW irradiance. In particular, we found that the increase of the SW and LW irradiance in the daytime favored on average the dilution of the fine mode particles and the accumulation of the coarse mode particles. Several processes may contribute to this effect. In particular, the irradiance could determine a vigorous and turbulent convection, which favors the mixing of the upper air enriched with coarse particles as the ones due to the long range transported African dust particles, with the air below containing mostly fine particles. The contribution of this process is expected to be significant mainly on dusty days. In fact, we found that the scattering Ångström coefficient reached a quite low value around midday on 6 May, since this day was quite affected by African dust particles. The irradiance increase, which likely favors more the dispersion of the fine mode particles than that of the coarse mode particles, being that the latter are on average “heavier” than fine mode particles, could also contribute to the coarse mode particle accumulation around midday. Finally, vehicles, which enhance

the re-suspension of road dust (large particles) into the air on the diurnal traffic rush hours, could also contributed to the decrease around midday as mentioned in some studies. It has also been shown that the night-time low values of the SW and LW irradiance favored the accumulation of particles at the surface. In conclusion, the large impact of the local SW and LW irradiance on the land-atmosphere interaction and particle dispersion at the surface was demonstrated under moderate aerosol load conditions and when the aerosol load was largely affected by the contribution of transboundary particles. We believe that the results in this paper have contributed to highlighting the relationships between SW and LW radiative fluxes and atmospheric particle properties. Consequently, they may be of some interest to better evaluate/understand the aerosol impact on climate.

Acknowledgments: S. Romano carried out this work with the support of a PhD fellowship from the Mathematics and Physics Department of the Salento University. The financial support for EARLINET in the ACTRIS Research Infrastructure Project by the European Union's Horizon 2020 research and innovation programme under grant agreement n. 654169 and previously under the grant agreement n. 262254 in the 7th Framework Programme (FP7/2007-2013) is gratefully acknowledged. The authors would like to acknowledge the Barcelona Super-Computing Center for the provision of the DREAM8b concentration profiles and the NOAA Air Resources Laboratory for the provision of the HYSPLIT back-trajectories. MODIS data were made available from the Goddard Laboratory sciences Data Center that is acknowledged.

Author Contributions: The authors have equally contributed to the work.

Conflicts of Interest: The authors declare no conflict of interest.

References

1. Perrone, M.R.; Romano, S.; Orza, J.A.G. Columnar and ground-level aerosol optical properties: Sensitivity to the transboundary pollution, daily and weekly patterns, and relationships. *Environ. Sci. Pollut. Res.* **2015**. [[CrossRef](#)] [[PubMed](#)]
2. Pandolfi, M.; Cusack, M.; Alastuey, A.; Querol, X. Variability of aerosol optical properties in the Western Mediterranean Basin. *Atmos. Chem. Phys.* **2011**, *11*, 8189–8203. [[CrossRef](#)]
3. Schuster, G.L.; Dubovik, O.; Holben, B.N. Ångström exponent and bimodal aerosol size distributions. *J. Geophys. Res.* **2006**, *111*, D07207. [[CrossRef](#)]
4. Lyamani, H.; Olmo, F.J.; Alados-Arboledas, L. Physical and optical properties of aerosols over an urban location in Spain: Seasonal and diurnal variability. *Atmos. Chem. Phys.* **2010**, *10*, 239–254. [[CrossRef](#)]
5. Pereira, S.N.; Wagner, F.; Silva, A.M. Seven year of measurements of aerosol scattering properties, near the surface, in the southwestern Iberia Peninsula. *Atmos. Chem. Phys.* **2011**, *11*, 17–29. [[CrossRef](#)]
6. Perrone, M.R.; Romano, S.; Orza, J.A.G. Particle optical properties at a Central Mediterranean site: Impact of advection routes and local meteorology. *Atmos. Res.* **2014**, *145–146*, 152–167. [[CrossRef](#)]
7. Betts, A.K.; Ball, J.H.; Beljaars, A.C.M.; Miller, M.J.; Viterbo, P.A. The land surface-atmosphere interaction: A review based on observational and global modeling perspective. *J. Geophys. Res.* **1996**, *101*, 7209–7225.
8. Holben, B.N.; Eck, T.F.; Slutsker, I.; Tanré, D.; Buis, J.P.; Setzer, A.; Vermote, E.; Reagan, J.A.; Kaufman, Y.J.; Nakajima, T.; *et al.* AERONET—A federated instrument network and data archive for aerosol characterization. *Remote Sens. Environ.* **1998**, *66*, 1–16. [[CrossRef](#)]
9. Basart, S.; Pérez, C.; Nickovic, S.; Cuevas, E.; Baldasano, J.M. Development and evaluation of the BSC-DREAM8b dust regional model over Northern Africa, the Mediterranean and the Middle East. *Tellus. B* **2012**. [[CrossRef](#)]
10. Perrone, M.R.; Becagli, S.; Orza, J.A.G.; Vecchi, R.; Dinoi, A.; Udisti, R.; Cabello, M. The impact of long-range-transport on PM₁ and PM_{2.5} at a Central Mediterranean site. *Atmos. Environ.* **2013**, *71*, 176–186. [[CrossRef](#)]
11. Müller, T.; Henzing, J.S.; de Leeuw, G.; Wiedensohler, A. Design and performance of a three-wavelength LED-based total scatter and backscatter integrating nephelometer. *Atmos. Meas. Tech.* **2011**, *4*, 1291–1303. [[CrossRef](#)]
12. King, M.D.; Kaufman, Y.J.; Menzel, W.P.; Tanré, D. Remote sensing of cloud, aerosol, and water vapor properties from the Moderate Resolution Imaging Spectrometer (MODIS). *IEEE Trans. Geosci. Remote Sens.* **1992**. [[CrossRef](#)]

13. Draxler, R.R.; Hess, G.D. An overview of the HYSPLIT_4 modeling system of trajectories, dispersion, and deposition. *Aust. Meteorol. Mag.* **1998**, *47*, 295–308.
14. Dubovik, O.; Sinyuk, A.; Lapyonok, T.; Holben, N.B.; Mishchenko, M.; Yang, P.; Eck, T.F.; Volten, H.; Munoz, O.; Veihelmann, B.; *et al.* Application of spheroid models to account for aerosol particle nonsphericity in remote sensing of desert dust. *J. Geophys. Res.: Atmos.* **2006**, *111*, D11208. [[CrossRef](#)]
15. Pavese, G.; De Tomasi, F.; Calvello, M.; Esposito, F.; Perrone, M.R. Detection of Sahara dust intrusions during mixed advection patterns over southeast Italy: A case study. *Atmos. Res.* **2009**, *92*, 489–504. [[CrossRef](#)]
16. Bergamo, A.; Tafuro, A.M.; Kinne, S.; De Tomasi, F.; Perrone, M.R. Monthly-averaged anthropogenic aerosol direct radiative forcing over the Mediterranean based on AERONET aerosol properties. *Atmos. Chem. Phys.* **2008**, *8*, 6995–7014. [[CrossRef](#)]
17. Romano, S.; Burlizzi, P.; Perrone, M.R. Experimental determination of short- and long-wave dust radiative effects in the Central Mediterranean and comparison with model results. *Atmos. Res.* **2015**. (submitted).
18. Hansell, R.A.; Tsay, S.C.; Ji, Q.; Hsu, N.C.; Jeong, M.J.; Wang, S.H.; Reid, J.S.; Liou, K.N.; Ou, S.C. An assessment of the surface longwave direct radiative effect of airborne Saharan dust during the NAMMA field campaign. *J. Atmos. Sci.* **2010**, *67*, 1048–1065. [[CrossRef](#)]
19. Sicard, M.; Bertolín, S.; Mallet, M.; Dubuisson, P.; Comerón, A. Estimation of mineral dust long-wave radiative forcing: Sensitivity study to particle properties and application to real cases in the region of Barcelona. *Atmos. Chem. Phys.* **2014**, *14*, 9213–9231. [[CrossRef](#)]
20. Stone, R.S.; Augustine, J.A.; Dutton, E.G.; O'Neill, N.T.; Saha, A. Empirical determination of the longwave and shortwave radiative forcing efficiencies of wildfire smoke. *J. Geophys. Res.* **2011**, *116*, D12207. [[CrossRef](#)]



© 2015 by the authors; licensee MDPI, Basel, Switzerland. This article is an open access article distributed under the terms and conditions of the Creative Commons by Attribution (CC-BY) license (<http://creativecommons.org/licenses/by/4.0/>).